HOKKAIDO UNIVERSITY

| | |
|---|---|
| Title | Quantitative imaging of pO2 in orthotopic murine gliomas : hypoxia correlates with resistance to radiation |
| Author(s) | Yasui, Hironobu; Kawai, Tatsuya; Matsumoto, Shingo et al. |
| Citation | Free Radical Research, 51(9-10), 861-871<br>https://doi.org/10.1080/10715762.2017.1388506 |
| Issue Date | 2017 |
| Doc URL | https://hdl.handle.net/2115/71782 |
| Rights | This is an Accepted Manuscript of an article published by Taylor & Francis in Free Radical Research in 2017, available online: http://www.tandfonline.com/10.1080/10715762.2017.1388506. |
| Type | journal article |
| File Information | FreeRadicRes51_861.pdf |

Hokkaido University Collection of Scholarly and Academic Papers : HUSCAP

**Quantitative imaging of pO2 in orthotopic murine gliomas: Hypoxia correlates with resistance to radiation.**

**Authors:**

Hironobu Yasui[1**] yasui@ric.hokudai.ac.jp
Tatsuya Kawai[2**] tatsuya.kawai@nih.gov
Shingo Matsumoto[3] smatsumoto@ist.hokudai.ac.jp
Keita Saito[4] Keita.Saito@nih.gov
Nallathamby Devasahayam[4] deva@helix.nih.gov
James B. Mitchell[4] jbm@helix.nih.gov
Kevin Camphausen[2] camphauk@mail.nih.gov
Osamu Inanami[5] inanami@vetmed.hokudai.ac.jp
Murali C. Krishna[4***] murali@helix.nih.gov

**These authors (Hironobu Yasui and Tatsuya Kawai) contributed equally to this work.
***Corresponding author

[1]Central Institute of Isotope Science, Hokkaido University
Kita 15, Nishi 7, Kita-ku, Sapporo, 060-0815 JAPAN

[2]Radiation Oncology Branch, Center for Cancer Research, National Cancer Institute, National Health Institutes
10 Center Drive, Bethesda, MD 20852

[3]Division of Bioengineering and Bioinformatics, Graduate School of Information Science and Technology, Hokkaido University
Kita 14, Nishi 9, Kita-ku, Sapporo 060-0814 JAPAN

[4]Radiation Biology Branch, Center for Cancer Research, National Cancer Institute, National Health Institutes
10 Center Drive, Bethesda, MD 20852

[5]Laboratory of Radiation Biology, Department of Environmental Veterinary Sciences, Graduate School of Veterinary Medicine, Hokkaido University
Kita 18, Nishi 9, Kita-ku, Sapporo 060-0818, JAPAN

**Key words** Glioma, Electron paramagnetic resonance imaging, hypoxia, radiation
**Running title** Quantitative imaging of pO2 in orthotopic gliomas

**Abstract**

Hypoxia is considered one of microenvironmental factors associated with the malignant nature of glioblastoma. Thus, evaluating intratumoral distribution of hypoxia would be useful for therapeutic planning as well as assessment of its effectiveness during the therapy. Electron paramagnetic resonance imaging (EPRI), is an imaging technique which can generate quantitative maps of oxygen *in vivo* using the exogenous paramagnetic compound, triarylmethyl and monitoring its line broadening caused by oxygen. In this study, the feasibility of EPRI for assessment of oxygen distribution in the glioblastoma using orthotopic U87 and U251 xenograft model. Heterogeneous distribution of $pO_2$ between 0 and 50 mmHg was observed throughout the tumors except for the normal brain tissue. U251 glioblastoma was more likely to exhibit hypoxia than U87 for comparable tumor size (median $pO_2$; 29.7 mmHg and 18.2 mmHg, $P = 0.028$, in U87 and U251, respectively). The area with $pO_2$ under 10 mmHg on the EPR oximetry (HF10) showed a good correlation with pimonidazole staining among tumors with evaluated size. In subcutaneous xenograft model, irradiation was relatively less effective for U251 compared to U87. In conclusion, EPRI is a feasible method to evaluate oxygen distribution in the brain tumor.

## Introduction

Glioblastoma (glioblastoma multiforme, GBM) is one subtype of gliomas that arise from glial or precursor cells and the most frequent primary malignant brain tumor in the Unites States with the incidence of 16% among all primary CNS neoplasms [1]. The prognosis of GBM is generally poor with a median survival of approximately 15 months even when treated with optimal therapy [2]. Similar to other malignant tumors, hypoxia is considered one of microenvironmental factors associated with the rapid tumor growth, progression, and resistance to conventional therapies including radiation therapy *via* an increase in expression of hypoxia-inducible factors (HIFs) [3, 4]. Recently, strategies of hypoxia-targeting cancer therapy such as bioreductive hypoxic toxins and small molecule inhibitors against hypoxia-specific molecular target, have been presented to overcome the refractory state of malignant tumors [5]. Thus, it would be useful for treatment of glioblastomas to evaluate intratumoral distribution of hypoxia for determining the therapeutic planning as well as assessment of its effectiveness during the therapy. In fact, positron emission tomography (PET) with a hypoxic tracer [$^{18}$F]-FMISO has been proven to be a prospective diagnostic tool for determining tumor aggressiveness in glioma patients and for predicting patient's prognosis [6, 7]. Furthermore, [$^{18}$F]-FMISO PET also could evaluate the efficacy of the antiangiogenic reagent sunitinib or a hypoxia-activated prodrug evofosfamide (TH-302) and to predict response to them in rat orthotropic glioma models C6 and 9L which show different hypoxic environment [8, 9]. The other hypoxic imaging technique, blood oxygen level-dependent (BOLD) MRI has been implemented in the clinic and relative oxygen extraction fraction (rOEF) map obtained from this method partly reflected the hypoxic

tumor region in glioma patient [10]. Both imaging techniques are noninvasive and safe enough to obtain information of tissue oxygenation from patients, but have limitation that they are not capable of absolute oxygen quantification nor necessarily correspond to each other [11].

Electron paramagnetic resonance imaging (EPRI) is an imaging technique similar to MRI. While MRI detects nuclear spins, EPRI detects unpaired electron spins of free radical species [12]. The EPR spectral line width of the paramagnetic trityl (TAM) is broadened by the collisional interaction with the surrounding dissolved paramagnetic oxygen. This change is proportional to oxygen concentration and can be correlated to absolute $pO_2$ value, enabling the quantitative oxygen concentration mapping of *in vivo* tissue. Development of EPR capabilities made it possible to obtain $pO_2$ maps with resolution of 3 to 4 mm Hg in three dimensions with a spatial resolution of ~1 to 2 mm [13]. Furthermore, establishment of combined system with EPR and MRI, operating at a common frequency such as 300 MHz with the corresponding magnetic fields at 10 mT (EPRI) and 7 T (MRI) enables $pO_2$ maps with anatomic guidance by sequential scans with the two modalities employing a common resonator [14]. Previous reports showed feasibility of $pO_2$ mapping created by EPRI in subcutaneous xenograft models using mice [15, 16]. Since many primary intracranial tumors are fed by the blood supply unique to central nervous system and their microvasculature is different from ectopic xenograft model, it might be more practical to assess the intratumoral oxygen level using orthotopic models [17]. Here we present the first study of EPRI for assessment of oxygen distribution in two different glioblastoma lines implanted in the mouse brain. We successfully showed the difference in intratumoral $pO_2$ map between the two glioblastoma lines and confirmed its validity by comparison to immunohistological

findings including a hypoxic probe pimonidazole along with an assessment of anaerobic metabolism-related markers, carbonic anhydrase 9 (CA-IX).

## Materials and Methods

### Chemicals

Evans Blue was purchased from Sigma Aldrich (St. Louis, MO). The triarylmethyl EPR oxygen tracer OX063 (methyl-tris[8-carboxy-2,2,6,6-tetrakis[(2-hydroxyethyl]-benzo[1,2-d:4,5-d′]bis[1,3]dithiol-4-yl] trisodium salt) was obtained from GE Healthcare（Pittsburgh, PA).

### Cell lines and *in vivo* tumor model.

The human glioma cell lines U87 and U251 (American Type Culture Collection, Gaithersburg, MD) were grown in DMEM and 10% fetal bovine serum at 37°C in 5% $CO_2$ and 95% room air. Athymic nude mice (nu/nu, female, 6-8 week of age, National Cancer Institute-Frederick Animal Production Area, Frederick, MD) were used. For intracranial tumor model, each mouse was anesthetized by a subcutaneous injection of ketamine (83 mg/kg) and xylazine (8.3 mg/kg) dissolved in saline prior to surgical procedures. Tumor cells ($1 \times 10^6$ cells) in a total volume of 5 μL were injected at 1.0 mm anterior and 2.0 mm lateral to the bregma to a depth of 3.0mm at a rate of approximately 1 μL/min. For subcutaneous model, tumor cells ($5 \times 10^5$ cells) in a total volume of 50 μL were injected subcutaneously into the right hind leg.

All animal experiments were carried out in compliance with the Guide for the care and use of laboratory animal resources (National Research Council, 1996) and the

experimental protocols were approved by the National Cancer Institute Animal Care and Use Committee.

**Imaging experiment**

Prior to imaging experiment, mice with an intracranial U87 or U251 tumor were injected with Evans Blue (1%, 200 µL bolus infusion) or OX063 (75 mM, 300 µL bolus infusion) *via* the tail vein and the excised and sliced brain tissues were observed in the bright field to confirm destruction of brain-blood barrier (BBB) at the tumor region.

A total of 12 mice (U87; n = 7, and U251; n = 5) were imaged 3-8 weeks after intracranial implantation of the tumor. Anatomic MRI was performed with ICON 1.0 T scanner controlled with ParaVision 5.0 (Bruker Bio-Spin MRI GmbH). After a quick assessment of the sample position by a fast low-angle shot (FLASH) pilot sequence, T2-weighted images (T2WI) were obtained using a fast spin echo sequence with an echo time (TE) of 85 msec, repetition time (TR) of 2,500 msec, 8 slices with 1 mm thickness, echo train length 8, number of average 12, field of volume 28 x 28 mm, in plane resolution 128 pixels, and acquisition time of 240 s.

For the EPR oxygen imaging, a custom-made EPRI scanner was used. Technical details of the EPRI scanner operating at 500 MHz, radio-frequency (RF) coil design, data acquisition based on the single point imaging (SPI) modality, image reconstruction, and the oxygen mapping procedure have been described in the earlier reports [14, 18, 19, 20, 21]. The mice were imaged immediately after an injection of OX063 (1.125 mmol/kg bolus infusion) *via* the tail vein cannulated with a 30-gauge needle. The acquisition parameters were as follows: Repetition time; 8 µs, 90-degree pulse; 20 ns, averager trigger; 0.350 µs, number of point; 640, input Range; 0.5, number

of total average; 4000, steps; 19 x 19 x 19, and gmh-gmm-gml; 1.4-1.14-0.96.

During the imaging experiments, mice were anaesthetized by isoflurane inhalation (4% for induction and 1-2% for maintaining anesthesia) and positioned prone with their heads placed inside the resonator. During EPRI and MRI measurements, the breathing rate of mouse was monitored with a pressure transducer (SA, Instruments Inc., Stony Brook, NY) and maintained at 60 ± 15 breaths per minutes. Core body temperature was monitored by a FISO FTI-10 temperature sensor (FISO Technologies Inc., Quebec, Canada) and maintained at 36°C±2°C with a flow of warm air for EPR imaging and with a warm water pad for MRI study.

**Irradiation and tumor growth study**

The experiments were initiated after when the subcutaneous tumors grew to approximately 200 $mm^3$ in volume (5 - 6 mm in diameter). Tumors were irradiated 2 Gy on days 0, 1 and 3 at a dose rate of 280.3 mGy/min (total 6 Gy) using a Pantak (Solon, OH) X-ray source. The animals were restrained without anaesthesia in a custom jig to be irradiated only on the tumor-bearing leg. The tumor size was measured on every 3-4 days with respect to the length, width and height directions by a digital caliper. All the measurements were duplicated to secure the accuracy.

**Immunohistochemistry**

For the hypoxic staining, pimonidazole (Natural Pharmacia International, Inc., Burlington, MA) was given to tumor-bearing mice intravenously according to the manufacturer's instruction 30 min before excising tumors. Tumor bearing mice were euthanized and perfused with 10 ml of 4 % paraformaldehyde. Tumor tissues were

excised from the brain and fixed with 4% paraformaldehyde overnight, frozen with Tissue-Tek® O.C.T. compound (Sakura Finetek U.S.A. Inc., Torrance, CA) on cold ethanol, and 10 μm thick sections were obtained. After blocking non-specific binding sites with serum-free protein block (Dako North America Inc., Carpinteria, CA), the slides were covered by rabbit anti-pimonidazole antisera (Hypoxyprobe Inc., Burlington, MA; 1:250) overnight at 4°C. The sections were incubated with FITC-conjugated anti-rabbit secondary antibody (Invitrogen, Carlsbad, CA; 1:500). Then they were mounted on Prolong Gold antifade reagent with DAPI (Invitrogen).

For CA-IX staining, slides were covered by rabbit anti-carbonic anhydrase IX antibody (AB15086; Abcam, Cambridge, MA; 1:1000) overnight at 4 °C followed by HRP-conjugated anti-rabbit antibody (sc-2004, Santa Cruz Biotechnology, Santa Cruz, CA; 1:1000), and were incubated in 0.3% $H_2O_2$ in TBS for 15 min. Fluorescence microscopic observation was performed using BZ9000 inverted fluorescent microscope (Keyence, Itasca, IL). The immunostaining-positive area was quantified using Image J software (NIH Image).

**Results**

*Histological and imaging characterization of the glioma cell lines U251 and U87*: To define the basic characters of two different glioblastoma cell lines, U87 and U251, MRI and immunohistochemical analyses were performed using orthotopic xenograft models in mice. As assessed by MRI, both tumors had a well-demarcated, high intensity area when compared to the normal brain parenchyma on FSE-T2WI (Figure 1A). The findings were similar between the two cell lines with the exception that the U251 tumor also had a higher intensity area surrounding the tumor, suggesting peri-tumoral edema, compared to the U87 tumor. On immunostaining for CA-IX and pimonidazole, the expression of CA-IX was significantly higher in U251 than U87 especially when the tumor size was larger than 50 $mm^3$. The CA-IX positive area was 15.9% vs. 2.3%, respectively (P = 0.034, Mann-Whitney's U test), and was less than 3.1% in all the U87 tumors evaluated in this study. The number of pimonidazole-positive cells was constantly higher in the U251 tumors than U87 (19.2% vs 9.1%, respectively; P = 0.012, Mann-Whitney's U test) even when the tumors were relatively small (Figure 1B and C). Although only U87 showed significant correlation between the tumor size and pimonidazole-positive area, apparent positive correlation in U87 and negative correlation in U251 were observed (R = 0.71, P = 0.049 for U87, and R = -0.53, P = 0.17 for U251). These histological studies suggest that the U251 tumor is more hypoxic than the U87.

*Tracer distribution in the U251 and U87 tumors:* Since effective uptake of the

oxygen-sensitive paramagnetic tracer OX063 into the tumor tissue is essential for the oxygen imaging by using EPRI, Evans Blue dye staining was performed to evaluate whether the blood brain barrier (BBB) was intact prior to the EPRI study. The Evans Blue dye was distributed throughout the tumor tissue in both tumor cell lines, indicating impairment of the BBB at the tumor site (Figure 2A, left). Similarly, distribution of OX063, which is green-colored reagent, was confirmed by macroscopical observation and intensity image of EPRI (Figure 2A, right and B). In contrast, the tracer was not distributed in the normal brain tissue, where BBB functioned properly (Figure 2B). These results show that OX063 accumulates in the orthotopic tumors at adequate levels to permit quantitative assessment of tumor $pO_2$.

*Oxygen mapping by EPR Imaging:* To investigate the difference in hypoxic status within the U87 and U251 orthotopic tumors, non-invasively, the spatial distribution of oxygen in the tumor-bearing mouse brain was examined using EPRI after administration of OX063 *via* the tail vein. Figure 3A shows axial (upper panel) and coronal (lower panel) planes of the oxygen maps from EPRI. These had a corresponding slice of 1-mm thickness T2-weighted MR image overlayed to give anatomical details. To assure accuracy of the cross-sectional locations between images from the two modalities, we use a sequential EPRI and MRI imaging system as described previously [14]. Heterogeneous distribution of $pO_2$ was observed in the range between 0 and 50 mmHg throughout the U87 and U251 tumors as well as the extracranial tissue except for the normal brain tissue. On the two-dimensional image where the size of the tumor section was largest, median $pO_2$ and the ratio of hypoxic area, where $pO_2$ was less than

10 mmHg (HF10) within the tumor were calculated to characterize tumor oxygen status for the two cell lines. The dot plot of HF10 against tumor volume suggest that the U251 glioblastoma was more hypoxic than U87 tumor in agreement with pimonidazole staining (Median $pO_2$, 29.7 mmHg (U87) vs. 18.2 mmHg (U251), P = 0.028, Mann-Whitney's U test). There was a significant positive correlation between the tumor size and HF10 in U251 (R = 0.94, P = 0.016) (Figure 3B).

*Growth delay by XRT*: To investigate the growth suppression effects of irradiation, subcutaneous xenograft tumor model was examined rather than the orthotopic tumor because it was possible to observe the tumor volume continuously until the tumor grew adequately large to evaluate. At 15 days (U87) or 4 days (U251) after an injection of tumor cell suspension, the tumor volume was calculated. Thereafter, the tumor was irradiated with 2 Gy dose per fraction for three consecutive days followed by measurement of the tumor size at every two to three days (Figure 4). To compensate different growth rate between the two cell lines by nature, the radioresponse ratio (relative growth delay) was calculated using the following equation:

Relative growth delay = [Days required to grow 500 $mm^3$ in X-rays group] / [ Days required to grow 500 $m^3$ in control group]

There was no significant difference in the tumor volume between the two lines and groups at the time point when the first irradiation was performed (P = 0.786). Tumor growth suppression was observed for both of the tumors compared to each non-irradiated control group, respectively. The relative growth delay was greater for

U87 than U251 although the absolute delay was shorter for U87 than U251 (Table 1).

## Discussion

To overcome the aggressive characteristics and therapeutic resistance that tumors acquire under hypoxic state within the intratumoral microenvironment is important [22, 23]. In clinical settings, evaluation of tumor hypoxia prior to treatment might be beneficial for designing optimal therapeutic strategies suitable for tumors in different oxygenation conditions. Previous studies showed potential effectiveness of dose escalation radiation therapy using [$^{18}$F]-FMISO PET to assess tumor hypoxia [24, 25]. The measurement of absolute $pO_2$ using [$^{18}$F]-FMISO PET, however, is not still sufficient to make quantitative delineations of hypoxic regions inside the tumor; this limitation might make it difficult to plan precisely for dose-modulation radiation therapy [26, 27]. On the other hand, a strong potential of EPRI for detection and quantitation of tumor hypoxia has also been shown using subcutaneous xenograft models in previous preclinical studies [14, 28]. EPRI is considered to have advantages over PET in some points where it is able to 1) measure $pO_2$ deep in tissue without radioisotopes, 2) to provide absolute $pO_2$ values with resolution of 3–4 mm Hg, and 3) is capable to obtain three-dimensional images of fluctuating oxygenation every 2–3 minutes with 1–2 mm spatial resolution.

In this study, we evaluated feasibility of EPRI for detecting hypoxic region in brain tumors by using an orthotopic xenograft mouse model and correlated the obtained $pO_2$ maps to histochemical findings of hypoxyprobe pimonidazole and CA-IX. CA-IX is one of the downstream proteins induced by HIF-1$\alpha$ and plays an essential role for maintaining intracellular pH under the metabolic shift to anaerobic glycolysis in hypoxic circumstances [29, 30]. We employed CA-IX as an indirect hypoxic marker because its

expression has been reported to closely correlate with tumor oxygenation by direct measurements using polarography [31, 32]. Besides, the amount of HIF-1α protein may not necessarily relate to oxygen level because its activity is tightly regulated, not only by rapid turnover when oxygen is abundant, but also by posttranslational modifications [33]. Pimonidazole is a widely-used hypoxic marker that binds to thiol-containing proteins specifically in hypoxic ($pO_2$ < 10 mmHg) cells and retains over hours in the tissue [34, 35, 36]. In general, BBB restricts the transport of hydrophilic or high molecular drugs into the brain to maintain the brain internal milieu and influences their distribution when we consider *in vivo* imaging of intracranial lesions using contrast materials [37, 38]. In previous reports, acceptable distribution of pimonidazole in the brain tumor as well as normal brain tissue has been described both in orthotopic xenograft models and human patients, indicating pimonidazole enters brain tissue through BBB [39, 40]. On the other hand, trityl OX063, a radical species used as a contrast agent for EPRI is a water-soluble large molecule (molecular mass; 1427) and its permeability through BBB remains unknown [41]. Generally, small (< 400 Da) nonpolar lipophilic agents are easily transported passively across the BBB, whereas hydrophilic compounds require active transport mechanisms [42, 43]. On the other hand, in many advanced malignant gliomas, disruption of the BBB was reported [44, 45]. The extravasation test of evans blue dye, which is known to bind to albumin producing a 68 kDa compound that does not cross the BBB [46], clearly showed that the leakage of evans blue dye into the tumor region compared to normal brain tissue, indicating the BBB disruption in both U87 and U251 intracranial tumors. Consistent with this observation, OX063 also showed a good distribution in the both tumors. This finding was consisted with the spin images derived from the incorporated OX063 on EPRI, suggested its validity for use of EPRI oximetry at

least in these tumor lines.

In the histological experiments, pimonidazole staining showed constantly higher in the ratio of positive areas within U251 than those within U87 except one tumor (Fig 1c, U87 in size 113.4 $mm^3$). Especially, the difference was more prominent when the tumor volume was small (< 10 $mm^3$). This finding along with our imaging finding on T2WI MRI was consistent with a former report that showed U87 xenografts were less infiltrative and exhibited profuse neovascularization without necrosis or hemorrhages compared to U251 [47]. Additionally, previous data that showed the density of microvasculature within the tumor as well as the expression level of VEGF were higher in U87 than U251 might also support our findings [48, 49]. Similarly, the expression of CA-IX in U251 was significantly higher than U87 when tumor volume was larger than 30 $mm^3$. In contrast to the pimonidazole staining, however, the expression of CA-IX remained low level in the both tumor lines when the tumor volume was small (< 20 $mm^3$). Rademakers et al. reported in their histochemical study of biopsy samples from human head and neck carcinomas that there were CA-IX-negative areas in pimonidazole staining area even though there was a correlation between the expression of these proteins [50]. Harada et al. also reported a discrepancy between pimonidazole-positive area and HIF-1α expression level and that this is because HIF-1α was dominantly suppressed in severe hypoxic and low-glucose area [51]. Combined with these knowledge, although still unclear, our results of CA-IX can be explained by assuming that an early-stage U251 tumor with smaller size has not developed enough tumor vessels so that severe hypoxic area was dominant and thus both HIF-1α and CA-IX expression remained low even in the pimonidazole-negative areas. Similarly, the case with pimonidazole-positive and low CA-IX-positive tumor in U87 could also be explained by those previous data. In contrast,

HF10, area with $pO_2$ under 10 mmHg on the EPR oximetry showed a similar tendency to pimonidazole staining among tumors with evaluated size. Especially, HF10 area in U87 on EPRI became higher in parallel with the increase in pimonidazole-positive area. There was also positive correlation between HF10 and the tumor size, consistent with former literature investigating hypoxic area using a modified comet assay [52].

Radiation sensitivity of these tumor lines was different in our subcutaneous xenograft model. The finding that U251 was more resistant to irradiation than U87 was reasonable in view of the result where hypoxic area was more dominant in the U251 tumor both in EPRI and pimonidazole findings. We employed the subcutaneous model which was of advantage that tumors could be tracked until they grow to relatively large size. However, the tumor sizes of both xenografts when the irradiation was performed were relatively large as about 150 $mm^3$; the formation of hypoxic region could occur in U87 tumor to some extent. This might influence the small difference of radioresponse ratio between two cell lines (1.45 for U87 vs 1.29 for U251). There were some limitations to be mentioned. First, it remained still unclear whether tumors without BBB disruption could be detected by EPRI. Although Shen et al. reported EPRI for brain ischemia using another radical compound that can cross BBB, there were also some limitations in sensitivity for $pO_2$ and its acquisition time [53]. Second, since this study did not compare EPRI findings and histochemistry in one-to-one manner, the exact localization of hypoxic areas on EPRI was not achieved. Third, a possibility of hypoxia-independent pimonidazole staining has been reported in some differentiated tumors especially in the region where reductive enzyme levels are elevated [54]. Fourth, small size tumors were not investigated on EPRI because of its limitation in spatial resolution. Nevertheless, a previous study using subcutaneous xenograft model successfully showed correlations

between the extent of hypoxia on EPRI $pO_2$ map and expression patterns of HIF-1α, suggesting this method could also be used for hypoxia mapping in the intracranial tumor [16]. Lastly, it has also been described the benefits of EPRI for investigating tumor metabolism by using along with other imaging modalities such as dynamic nuclear polarized MRI [55]. In conclusion, this is the first report that showed a feasibility of EPRI for the brain tumor using orthotopic brain tumor model and might provide not only information of malignancy or sensitivity to treatment but also help us obtain useful knowledge in metabolism of brain tumors that leads to more effective therapeutic strategies and excellent outcome.

**Figure legends**

Figure 1. Basic characteristics of two glioma lines.
FSE-T2WI shows well-demarcated, relatively hyperintense area. Note that U251 has an apparent peri-focal edema compared to U87 (A).
Immunohistochemistry for CA-IX (A; brown) and immunofluorescent for pimonidazole (B; green) in two different tumor examples are shown, one is small and the other is big. Red bars indicate 1-mm scale. Each of the tumor volumes is shown below the corresponding image. The dot-plot graph shows differences in the distribution pattern of CA-IX expression and the pimonidazole-positive hypoxic area between the two lines (C).

Figure 2. BBB disruption and tracer distribution.
Macroscopic view of the specimens after an injection of Evans Blue or OX063 show a good distribution of the dye within entire the tumor tissue in both of the tumor cell lines (A). T2WI (left) and EPRI overlaid on the corresponding T2WI (right) shows that EPR signal is detected from both the two different tumor and normal tissue (B). Solid lines indicate the boundaries of the tumors.

Figure 3. EPR oxygen mapping.
The color-coded $pO_2$ map overlaid on T2WI shows an apparent light blue area that indicates hypoxia in U251 tumor (A). For reference, the corresponding non-overlaid T2WI is shown along with each EPR $pO_2$ mapping. The tumor regions are indicated by green borders.
Dot-plot graphs of median $pO_2$ (B, left) and HF10 (B, right) against the tumor size showed a positive correlation between HF10 and tumor volume in the U251.

Figure 4. Growth delay by XRT.
Growth curves of subcutaneous xenograft of U87 and U251 after irradiation (dashed lines) and non-irradiated control (solid lines). The values are represented as the mean ± S.E. Each arrow indicates an irradiation with a dose of 2 Gy.

**References**


1. Ostrom QT, Gittleman H, Farah P, et al. CBTRUS statistical report: Primary brain and central nervous system tumors diagnosed in the United States in 2006-2010. Neuro-oncology. 2013 Nov;15 Suppl 2:ii1-56. doi: 10.1093/neuonc/not151. PubMed PMID: 24137015; PubMed Central PMCID: PMCPMC3798196. eng.
2. Tran B, Rosenthal MA. Survival comparison between glioblastoma multiforme and other incurable cancers. Journal of clinical neuroscience : official journal of the Neurosurgical Society of Australasia. 2010 Apr;17(4):417-21. doi: 10.1016/j.jocn.2009.09.004. PubMed PMID: 20167494; eng.
3. Joseph JV, Conroy S, Pavlov K, et al. Hypoxia enhances migration and invasion in glioblastoma by promoting a mesenchymal shift mediated by the HIF1alpha-ZEB1 axis. Cancer letters. 2015 Apr 01;359(1):107-16. doi: 10.1016/j.canlet.2015.01.010. PubMed PMID: 25592037; eng.
4. Yang L, Lin C, Wang L, et al. Hypoxia and hypoxia-inducible factors in glioblastoma multiforme progression and therapeutic implications. Experimental cell research. 2012 Nov 15;318(19):2417-26. doi: 10.1016/j.yexcr.2012.07.017. PubMed PMID: 22906859; eng.
5. Wilson WR, Hay MP. Targeting hypoxia in cancer therapy. Nature reviews Cancer. 2011 Jun;11(6):393-410. doi: 10.1038/nrc3064. PubMed PMID: 21606941; eng.
6. Hirata K, Terasaka S, Shiga T, et al. (1)(8)F-Fluoromisonidazole positron emission tomography may differentiate glioblastoma multiforme from less malignant gliomas. European journal of nuclear medicine and molecular imaging. 2012 May;39(5):760-70. doi: 10.1007/s00259-011-2037-0. PubMed PMID: 22307533; eng.
7. Spence AM, Muzi M, Swanson KR, et al. Regional hypoxia in glioblastoma multiforme quantified with [18F]fluoromisonidazole positron emission tomography before radiotherapy: correlation with time to progression and survival. Clinical cancer research : an official journal of the American Association for Cancer Research. 2008 May 01;14(9):2623-30. doi: 10.1158/1078-0432.ccr-07-4995. PubMed PMID: 18451225; PubMed Central PMCID: PMCPMC4415875. eng.
8. Stokes AM, Hart CP, Quarles CC. Hypoxia Imaging With PET Correlates With Antitumor Activity of the Hypoxia-Activated Prodrug Evofosfamide (TH-302)

in Rodent Glioma Models. Tomography : a journal for imaging research. 2016 Sep;2(3):229-237. doi: 10.18383/j.tom.2016.00259. PubMed PMID: 27752544; PubMed Central PMCID: PMCPMC5065246. eng.

9. Valable S, Petit E, Roussel S, et al. Complementary information from magnetic resonance imaging and (18)F-fluoromisonidazole positron emission tomography in the assessment of the response to an antiangiogenic treatment in a rat brain tumor model. Nuclear medicine and biology. 2011 Aug;38(6):781-93. doi: 10.1016/j.nucmedbio.2011.01.010. PubMed PMID: 21843775; eng.
10. Toth V, Forschler A, Hirsch NM, et al. MR-based hypoxia measures in human glioma. Journal of neuro-oncology. 2013 Nov;115(2):197-207. doi: 10.1007/s11060-013-1210-7. PubMed PMID: 23918147; eng.
11. Preibisch C, Shi K, Kluge A, et al. Characterizing hypoxia in human glioma: A simultaneous multimodal MRI and PET study. NMR Biomed. 2017 Aug 14. doi: 10.1002/nbm.3775. [Epub ahead of print]
12. Krishna MC, Subramanian S, Kuppusamy P, et al. Magnetic resonance imaging for in vivo assessment of tissue oxygen concentration. Seminars in radiation oncology. 2001 Jan;11(1):58-69. PubMed PMID: 11146043; eng.
13. Krishna MC, Matsumoto S, Yasui H, et al. Electron paramagnetic resonance imaging of tumor pO(2). Radiation research. 2012 Apr;177(4):376-86. PubMed PMID: 22332927; eng.
14. Matsumoto S, Hyodo F, Subramanian S, et al. Low-field paramagnetic resonance imaging of tumor oxygenation and glycolytic activity in mice. The Journal of clinical investigation. 2008 May;118(5):1965-73. doi: 10.1172/jci34928. PubMed PMID: 18431513; PubMed Central PMCID: PMCPMC2323191. eng.
15. Matsumoto S, Saito K, Takakusagi Y, et al. In vivo imaging of tumor physiological, metabolic, and redox changes in response to the anti-angiogenic agent sunitinib: longitudinal assessment to identify transient vascular renormalization. Antioxidants & redox signaling. 2014 Sep 10;21(8):1145-55. doi: 10.1089/ars.2013.5725. PubMed PMID: 24597714; PubMed Central PMCID: PMCPMC4142786. eng.
16. Matsumoto S, Saito K, Yasui H, et al. EPR oxygen imaging and hyperpolarized 13C MRI of pyruvate metabolism as noninvasive biomarkers of tumor treatment response to a glycolysis inhibitor 3-bromopyruvate. Magnetic resonance in medicine. 2013 May;69(5):1443-50. doi: 10.1002/mrm.24355. PubMed PMID: 22692861; PubMed Central PMCID: PMCPMC3479339. eng.

17. Dimberg A. The glioblastoma vasculature as a target for cancer therapy. Biochemical Society transactions. 2014 Dec;42(6):1647-52. doi: 10.1042/bst20140278. PubMed PMID: 25399584; eng.
18. Devasahayam N, Subramanian S, Murugesan R, et al. Parallel coil resonators for time-domain radiofrequency electron paramagnetic resonance imaging of biological objects. Journal of magnetic resonance (San Diego, Calif : 1997). 2000 Jan;142(1):168-76. doi: 10.1006/jmre.1999.1926. PubMed PMID: 10617448; eng.
19. Devasahayam N, Subramanian S, Murugesan R, et al. Strategies for improved temporal and spectral resolution in in vivo oximetric imaging using time-domain EPR. Magnetic resonance in medicine. 2007 Apr;57(4):776-83. doi: 10.1002/mrm.21194. PubMed PMID: 17390350; eng.
20. Matsumoto K, Subramanian S, Devasahayam N, et al. Electron paramagnetic resonance imaging of tumor hypoxia: enhanced spatial and temporal resolution for in vivo pO2 determination. Magnetic resonance in medicine. 2006 May;55(5):1157-63. doi: 10.1002/mrm.20872. PubMed PMID: 16596636; eng.
21. Subramanian S, Devasahayam N, Murugesan R, et al. Single-point (constant-time) imaging in radiofrequency Fourier transform electron paramagnetic resonance. Magnetic resonance in medicine. 2002 Aug;48(2):370-9. doi: 10.1002/mrm.10199. PubMed PMID: 12210946; eng.
22. Begg AC, Stewart FA, Vens C. Strategies to improve radiotherapy with targeted drugs. Nature reviews Cancer. 2011 Apr;11(4):239-53. doi: 10.1038/nrc3007. PubMed PMID: 21430696; eng.
23. Fokas E, McKenna WG, Muschel RJ. The impact of tumor microenvironment on cancer treatment and its modulation by direct and indirect antivascular strategies. Cancer metastasis reviews. 2012 Dec;31(3-4):823-42. doi: 10.1007/s10555-012-9394-4. PubMed PMID: 22825313; eng.
24. Hendrickson K, Phillips M, Smith W, et al. Hypoxia imaging with [F-18] FMISO-PET in head and neck cancer: potential for guiding intensity modulated radiation therapy in overcoming hypoxia-induced treatment resistance. Radiotherapy and oncology : journal of the European Society for Therapeutic Radiology and Oncology. 2011 Dec;101(3):369-75. doi: 10.1016/j.radonc.2011.07.029. PubMed PMID: 21872957; PubMed Central PMCID: PMCPMC3225491. eng.
25. Welz S, Monnich D, Pfannenberg C, et al. Prognostic value of dynamic hypoxia PET in head and neck cancer: Results from a planned interim analysis of a

randomized phase II hypoxia-image guided dose escalation trial. Radiotherapy and oncology : journal of the European Society for Therapeutic Radiology and Oncology. 2017 Apr 20. doi: 10.1016/j.radonc.2017.04.004. PubMed PMID: 28434798; eng.

26. Mahling M, Fuchs K, Thaiss WM, et al. A Comparative pO2 Probe and [18F]-Fluoro-Azomycinarabino-Furanoside ([18F]FAZA) PET Study Reveals Anesthesia-Induced Impairment of Oxygenation and Perfusion in Tumor and Muscle. PloS one. 2015;10(4):e0124665. doi: 10.1371/journal.pone.0124665. PubMed PMID: 25902054; PubMed Central PMCID: PMCPMC4406741. eng.
27. Monnich D, Welz S, Thorwarth D, et al. Robustness of quantitative hypoxia PET image analysis for predicting local tumor control. Acta oncologica (Stockholm, Sweden). 2015;54(9):1364-9. doi: 10.3109/0284186x.2015.1071496. PubMed PMID: 26481464; eng.
28. Elas M, Ahn KH, Parasca A, et al. Electron paramagnetic resonance oxygen images correlate spatially and quantitatively with Oxylite oxygen measurements. Clinical cancer research : an official journal of the American Association for Cancer Research. 2006 Jul 15;12(14 Pt 1):4209-17. doi: 10.1158/1078-0432.ccr-05-0446. PubMed PMID: 16857793; eng.
29. Giatromanolaki A, Koukourakis MI, Sivridis E, et al. Expression of hypoxia-inducible carbonic anhydrase-9 relates to angiogenic pathways and independently to poor outcome in non-small cell lung cancer. Cancer research. 2001 Nov 01;61(21):7992-8. PubMed PMID: 11691824; eng.
30. Parks SK, Chiche J, Pouyssegur J. pH control mechanisms of tumor survival and growth. Journal of cellular physiology. 2011 Feb;226(2):299-308. doi: 10.1002/jcp.22400. PubMed PMID: 20857482; eng.
31. Loncaster JA, Harris AL, Davidson SE, et al. Carbonic anhydrase (CA IX) expression, a potential new intrinsic marker of hypoxia: correlations with tumor oxygen measurements and prognosis in locally advanced carcinoma of the cervix. Cancer research. 2001 Sep 01;61(17):6394-9. PubMed PMID: 11522632; eng.
32. Potter CP, Harris AL. Diagnostic, prognostic and therapeutic implications of carbonic anhydrases in cancer. British journal of cancer. 2003 Jul 07;89(1):2-7. doi: 10.1038/sj.bjc.6600936. PubMed PMID: 12838292; PubMed Central PMCID: PMCPMC2394207. eng.
33. Lee JW, Bae SH, Jeong JW, et al. Hypoxia-inducible factor (HIF-1)alpha: its protein stability and biological functions. Experimental & molecular medicine.

2004 Feb 29;36(1):1-12. doi: 10.1038/emm.2004.1. PubMed PMID: 15031665; eng.

34. Busk M, Jakobsen S, Horsman MR, et al. PET imaging of tumor hypoxia using 18F-labeled pimonidazole. Acta oncologica (Stockholm, Sweden). 2013 Oct;52(7):1300-7. doi: 10.3109/0284186x.2013.815797. PubMed PMID: 23962243; eng.
35. Chou SC, Azuma Y, Varia MA, et al. Evidence that involucrin, a marker for differentiation, is oxygen regulated in human squamous cell carcinomas. British journal of cancer. 2004 Feb 09;90(3):728-35. doi: 10.1038/sj.bjc.6601585. PubMed PMID: 14760391; PubMed Central PMCID: PMCPMC2409601. eng.
36. Gross MW, Karbach U, Groebe K, et al. Calibration of misonidazole labeling by simultaneous measurement of oxygen tension and labeling density in multicellular spheroids. International journal of cancer. 1995 May 16;61(4):567-73. PubMed PMID: 7759162; eng.
37. Abbott NJ, Patabendige AA, Dolman DE, et al. Structure and function of the blood-brain barrier. Neurobiology of disease. 2010 Jan;37(1):13-25. doi: 10.1016/j.nbd.2009.07.030. PubMed PMID: 19664713; eng.
38. Tabanor K, Lee P, Kiptoo P, et al. Brain Delivery of Drug and MRI Contrast Agent: Detection and Quantitative Determination of Brain Deposition of CPT-Glu Using LC-MS/MS and Gd-DTPA Using Magnetic Resonance Imaging. Molecular pharmaceutics. 2016 Feb 01;13(2):379-90. doi: 10.1021/acs.molpharmaceut.5b00607. PubMed PMID: 26705088; PubMed Central PMCID: PMCPMC4935662. eng.
39. Bernsen HJ, Rijken PF, Peters H, et al. Hypoxia in a human intracerebral glioma model. Journal of neurosurgery. 2000 Sep;93(3):449-54. doi: 10.3171/jns.2000.93.3.0449. PubMed PMID: 10969943; eng.
40. Newman HF, Bleehen NM, Ward R, et al. Hypoxic cell radiosensitizers in the treatment of high grade gliomas: a new direction using combined Ro 03-8799 (pimonidazole) and SR 2508 (etanidazole). International journal of radiation oncology, biology, physics. 1988 Sep;15(3):677-84. PubMed PMID: 2843488; eng.
41. Lumata L, Kovacs Z, Sherry AD, et al. Electron spin resonance studies of trityl OX063 at a concentration optimal for DNP. Physical chemistry chemical physics : PCCP. 2013 Jun 28;15(24):9800-7. doi: 10.1039/c3cp50186h. PubMed PMID: 23676994; PubMed Central PMCID: PMCPMC3698225. eng.
42. Loscher W, Potschka H. Drug resistance in brain diseases and the role of drug

efflux transporters. Nature reviews Neuroscience. 2005 Aug;6(8):591-602. doi: 10.1038/nrn1728. PubMed PMID: 16025095; eng.

43. Pardridge WM. Blood-brain barrier drug targeting: the future of brain drug development. Molecular interventions. 2003 Mar;3(2):90-105, 51. doi: 10.1124/mi.3.2.90. PubMed PMID: 14993430; eng.
44. Deeken JF, Loscher W. The blood-brain barrier and cancer: transporters, treatment, and Trojan horses. Clinical cancer research : an official journal of the American Association for Cancer Research. 2007 Mar 15;13(6):1663-74. doi: 10.1158/1078-0432.ccr-06-2854. PubMed PMID: 17363519; eng.
45. Schneider SW, Ludwig T, Tatenhorst L, et al. Glioblastoma cells release factors that disrupt blood-brain barrier features. Acta neuropathologica. 2004 Mar;107(3):272-6. doi: 10.1007/s00401-003-0810-2. PubMed PMID: 14730455; eng.
46. Rapoport SI. Osmotic opening of the blood-brain barrier: principles, mechanism, and therapeutic applications. Cellular and molecular neurobiology. 2000 Apr;20(2):217-30. PubMed PMID: 10696511; eng.
47. Candolfi M, Curtin JF, Nichols WS, et al. Intracranial glioblastoma models in preclinical neuro-oncology: neuropathological characterization and tumor progression. Journal of neuro-oncology. 2007 Nov;85(2):133-48. doi: 10.1007/s11060-007-9400-9. PubMed PMID: 17874037; PubMed Central PMCID: PMCPMC2384236. eng.
48. Corroyer-Dulmont A, Pérès EA, Petit E, et al. Noninvasive assessment of hypoxia with 3-[18F]-fluoro-1-(2-nitro-1-imidazolyl)-2-propanol ([18F]-FMISO): a PET study in two experimental models of human glioma. Biol Chem. 2013 Apr;394(4):529-39. doi: 10.1515/hsz-2012-0318.
49. Hovinga KE, Stalpers LJ, van Bree C, et al. Radiation-enhanced vascular endothelial growth factor (VEGF) secretion in glioblastoma multiforme cell lines--a clue to radioresistance? Journal of neuro-oncology. 2005 Sep;74(2):99-103. doi: 10.1007/s11060-004-4204-7. PubMed PMID: 16193379; eng.
50. Rademakers SE, Lok J, van der Kogel AJ, et al. Metabolic markers in relation to hypoxia; staining patterns and colocalization of pimonidazole, HIF-1alpha, CAIX, LDH-5, GLUT-1, MCT1 and MCT4. BMC cancer. 2011 May 12;11:167. doi: 10.1186/1471-2407-11-167. PubMed PMID: 21569415; PubMed Central PMCID: PMCPMC3115911. eng.
51. Harada H, Inoue M, Itasaka S, et al. Cancer cells that survive radiation therapy

acquire HIF-1 activity and translocate towards tumour blood vessels. Nature communications. 2012 Apr 17;3:783. doi: 10.1038/ncomms1786. PubMed PMID: 22510688; PubMed Central PMCID: PMCPMC3337987. eng.

52. Wang J, Klem J, Wyrick JB, et al. Detection of hypoxia in human brain tumor xenografts using a modified comet assay. Neoplasia (New York, NY). 2003 Jul-Aug;5(4):288-96. doi: No_doi. PubMed PMID: 14511400; PubMed Central PMCID: PMCPMC1502416. eng.

53. Shen J, Sood R, Weaver J, et al. Direct visualization of mouse brain oxygen distribution by electron paramagnetic resonance imaging: application to focal cerebral ischemia. Journal of cerebral blood flow and metabolism : official journal of the International Society of Cerebral Blood Flow and Metabolism. 2009 Oct;29(10):1695-703. doi: 10.1038/jcbfm.2009.89. PubMed PMID: 19675560; PubMed Central PMCID: PMCPMC3633216. eng.

54. Janssen HL, Hoebers FJ, Sprong D, et al. Differentiation-associated staining with anti-pimonidazole antibodies in head and neck tumors. Radiother Oncol. 2004 Jan;70(1):91-7.

55. Krishna MC, Matsumoto S, Saito K, et al. Magnetic resonance imaging of tumor oxygenation and metabolic profile. Acta oncologica (Stockholm, Sweden). 2013 Oct;52(7):1248-56. doi: 10.3109/0284186x.2013.819118. PubMed PMID: 23957619; eng.

# Fig. 1 Basic characters of 2 human glioma lines

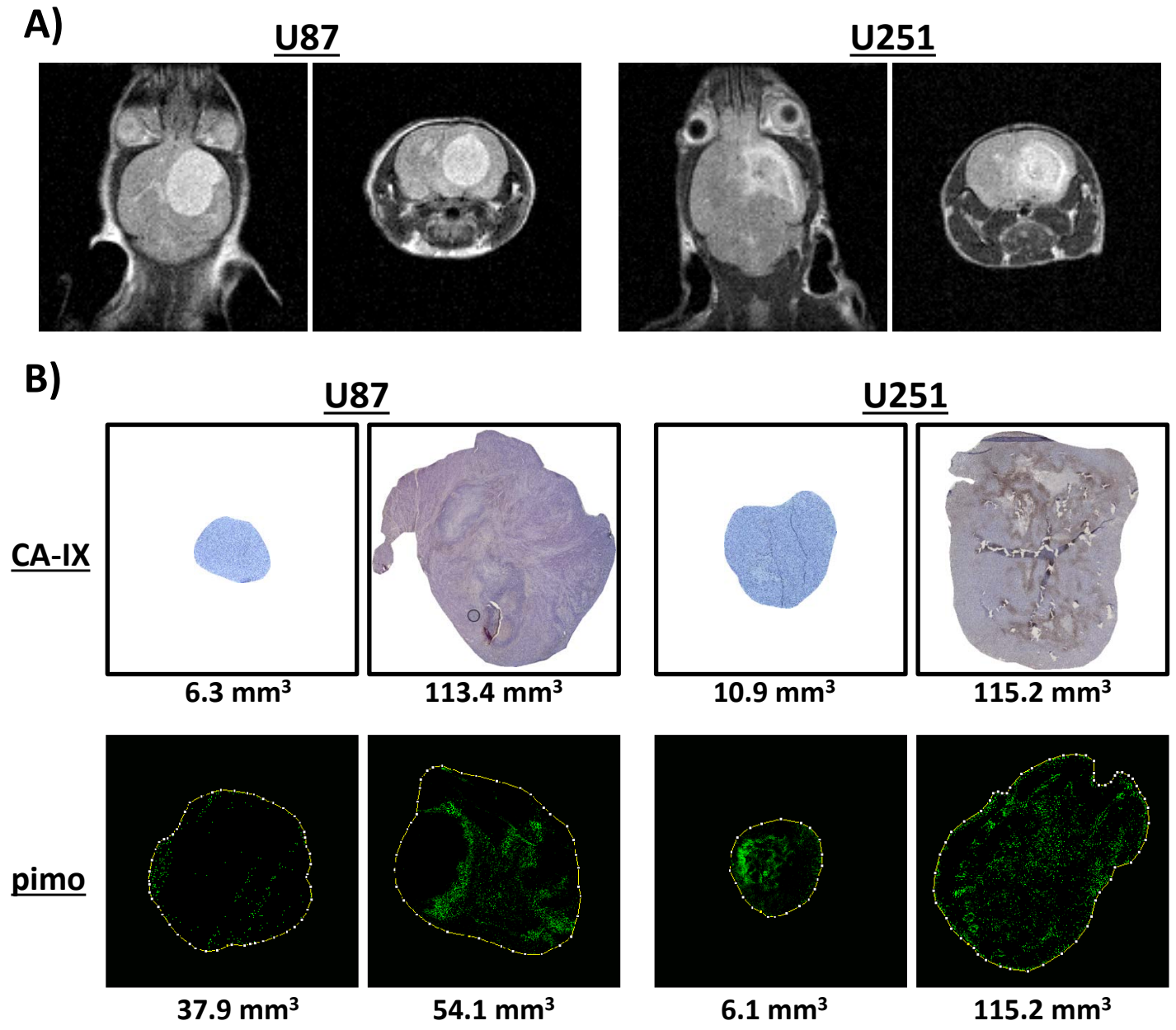


C)

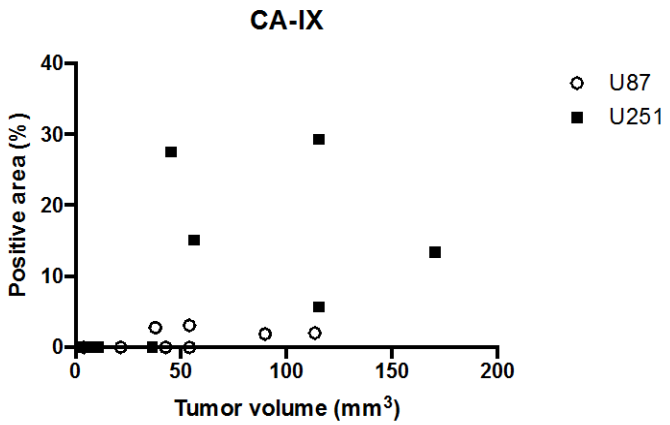


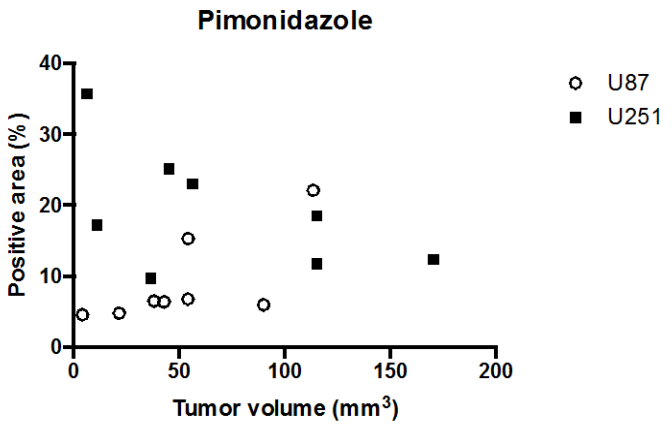

# Fig. 2 Tracer distribution after BBB disruption

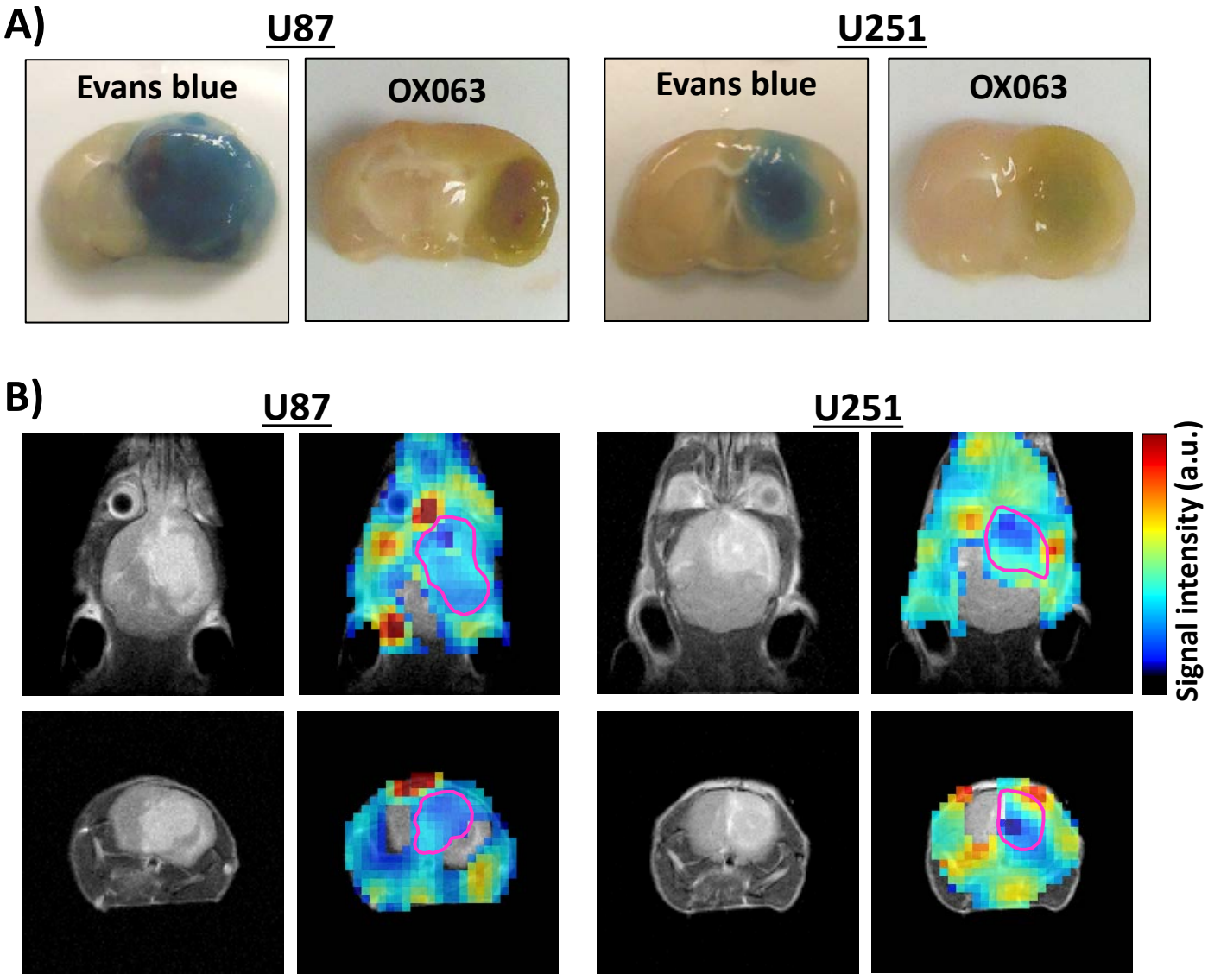

# Fig. 3 Oxygen mapping

A)

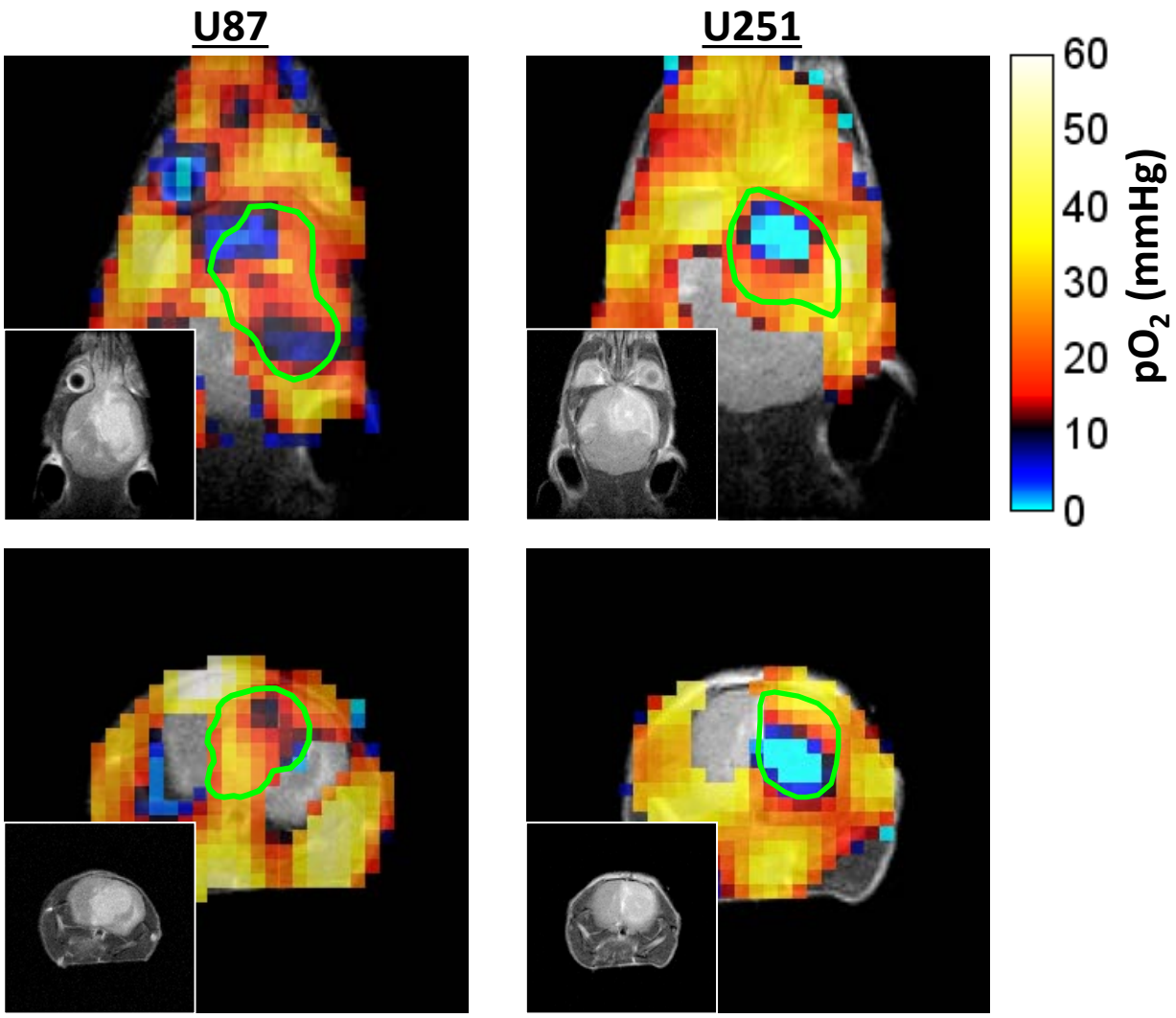


B)

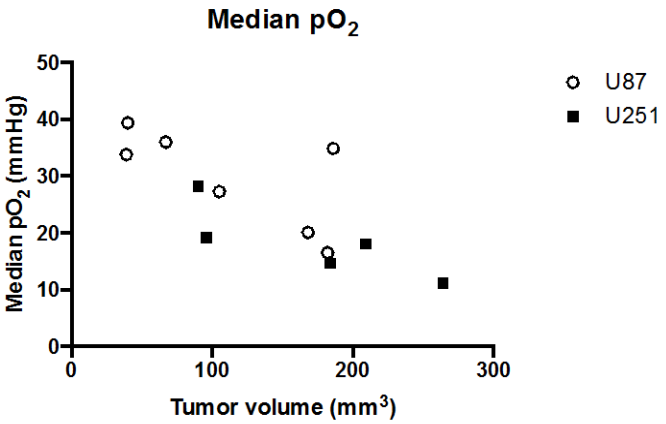


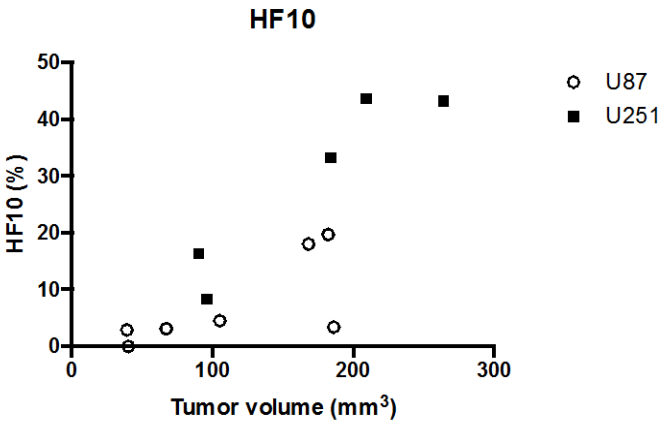

# Fig. 4 Growth delay by XRT

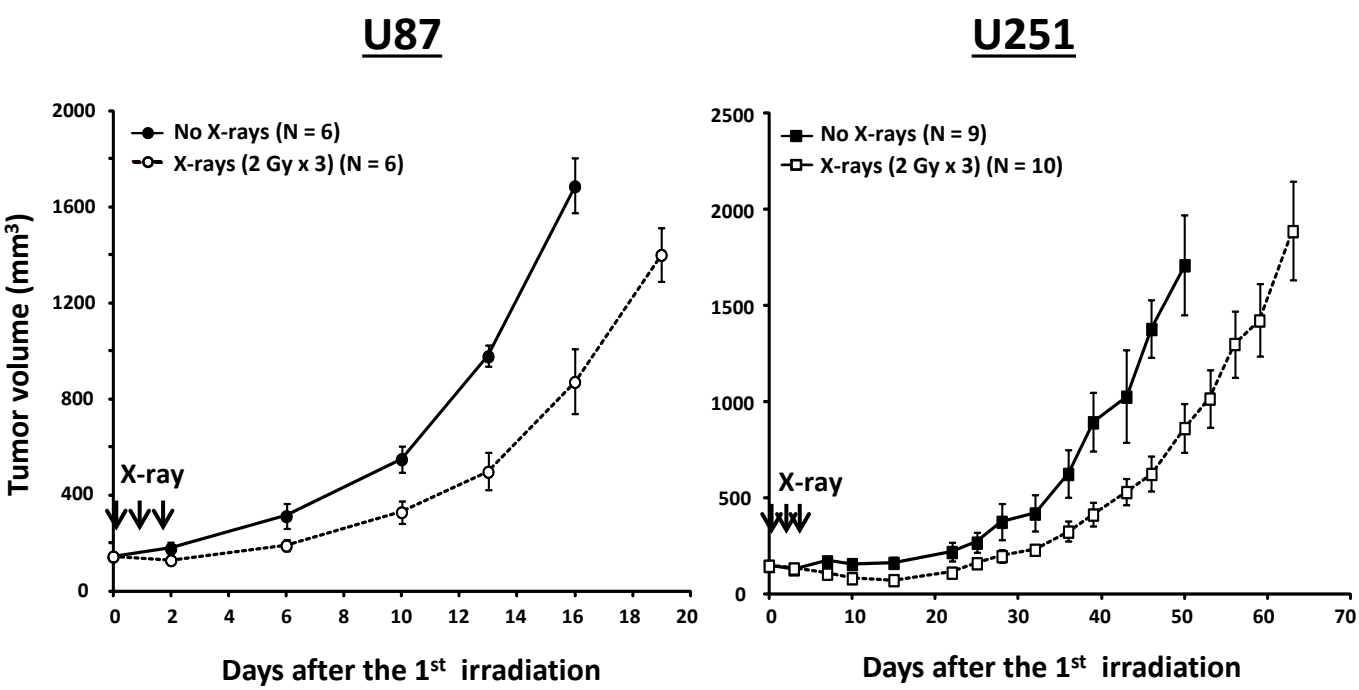

| Cell line | Irradiation | # of mice | Tumor volume in the day of first irradiation | Time in days required to grow to 500 $mm^3$ | Absolute delay | Radioresponse ratio (Relative growth delay*) |
|---|---|---|---|---|---|---|
| U87 | No X-rays | 6 | 145.7±18.5 | 10.3±2.6 | 4.7 | 1.45 |
| | X-rays (2 Gy x 3) | 6 | 146.4±17.4 | 15.0±2.4 | | |
| U251 | No X-rays | 9 | 145.4±27.4 | 34.4±6.9 | 10.1 | 1.29 |
| | X-rays (2 Gy x 3) | 10 | 148.4±26.4 | 44.5±7.9 | | |

Table 1.

Summary of the tumor growth. Note that relative growth delay was greater for U87 than U251 although the absolute delay was shorter for U87 than U251.